Heritage Science

RESEARCH

Open Access

Corrosion analysis of unearthed jade from Daye Zhen Tomb of Northern Zhou Dynasty

Kexin Zhang[1,2†], Yaxu Zhang[3,4,5†], Jing Zhao[2*], Zhanrui Zhao[3,4,5], Meng Zhao[1,2], Xichen Zhao[3,4,5*] and Hongjie Luo[2]

Abstract

X-ray fluorescence spectroscopy, scanning electron microscopy energy spectrum, excitation-emission matrix spectroscopy, and Fourier transform infrared spectroscopy was applied to the unearthed jade with multilayered corrosion, to reveal the microstructure, composition structure, and distribution of organic matters. Our results showed that the interior of the jade was mainly composed of layered serpentine with a regular structure, while the white layer structure on the surface is scattered and irregular, and the content of calcite formed by elements Ca and C increases significantly; between the green matrix and the white layer on the surface, there are brown corrosion zones with obvious fluorescence effect and mainly composed of humic acid, which continuously extends inward along the corrosion cracks for accelerating the internal corrosion. This article, for the first time, argued for the corrosive and fluorescent humic acid bands that appear inside serpentine jade and cautions its role in investigating the corrosion of jade.

Keywords Jade, Serpentine, Fluorescence effect, Humic acid zone, Corrosion model

Introduction

In China, jade is highly valued for its practical uses (as ornaments and tools) and crucial role in religion, etiquette, and other occasions [1]. The earliest jade in China was found at Xiaonanshan Site (小南山) in Raohe County, Heilongjiang Province (9200–8600 BP). Jade, as defined by modern geology and gemology, refers to two extremely tough, essentially monomin-eralic rocks that are used for fashioning ornamental carvings and gems, jade with narrow sense includes the nephrite $[Ca_2(Mg,Fe)_5[Si_4O_{11}]_2(OH)_2]$ and jadeite$[NaAlSi_2O_6]$ [2], although their compositions and textures differ, both types of jade are typically associated with serpentinite, which is a general term for a hydrated magnesia-rich silicate mineral. Serpentinite is replaced by Ca metasomatism to form nephrite in contacts with more siliceous rocks (plagiogranite, graywacke, argillite) [3]. At the same time, jadeite is formed as fluid crystallization-to-metasomatic product in the channel-wedge boundary of fossil subduction system of serpentine matrix [4]. Unearthed jade artifacts will change in different types and degrees in terms of color, transparency, luster, hardness and other characteristics. Among them, the whitened jade is a common phenomenon, and some results believe that it is due to the color change caused by burning, and the color

†Kexin Zhang and Yaxu Zhang contributed equally to this work and should be considered co-first authors.

*Correspondence:
Jing Zhao
zhaojing@mail.sic.ac.cn
Xichen Zhao
zxc0324@163.com
[1] School of Materials and Chemistry, University of Shanghai for Science and Technology, Shanghai 200093, China
[2] Shanghai Institute of Ceramics, Chinese Academy of Sciences, Shanghai 200050, China
[3] Shaanxi Institute of Archaeology, Xi'an 710054, China
[4] Key Scientific Research Base of On-site Conservation, State Administration for Cultural Heritage, Xi'an 710054, China
[5] Shaanxi Key Laboratory of Archaeological Conservation, Xi'an 710054, China

change of jade varies according to the burning temperature [5, 6].

As a silicate mineral, serpentine will also undergo corrosion during burial, such as surface hydroxylation of silicate minerals, that is, dissociated water molecules are adsorbed on the surface cation –O pair, the hydroxyl group binds to the surface cation, and the H atom binds to the surface O atom [7–9]. Subsequently, alkaline earth cations such as Ca^{2+} and Mg^{2+} are rapidly released from the surface of hydroxylated silicate minerals through proton exchange for H^{+} [7, 10], making silicate minerals susceptible to surface corrosion in acidic conditions and aqueous solutions [10–12]. In the natural environment, carbonate and silicate biomineralization is also a common phenomenon, and bacteria such as cyanobacteria and sulfate reducing bacteria attach to the surface of various mineral substrates, inducing carbonate precipitation, micron-sized crystals of low-Mg calcite are the most common products [13–16]. Extracellular polymeric substances (EPS), all organic molecules secreted by microorganisms [17], play a key role in accumulating cations and providing mineralization nucleation sites [18–22]. Some scholars have found that viruses may also cause mineralization [15, 23], and as the pathway of mineralization induced by microorganisms is very complex, the whole process has not been fully defined.

In 2021, the Shaanxi Academy of Archeology excavated the tomb of the nobleman Daye Zhen (大野贞) during the Northern Zhou Dynasty (557–581 AD) during the third phase of the reconstruction and expansion project of Xi'an Xianyang International Airport. The shape and structure of the tomb were fully preserved, with rich funerary objects. Furthermore, a large number of painted pottery figurines, gold and silver wares, and other precious cultural relics were unearthed. Among them, a set of jade ornaments, including a Jade *Heng* pendant, Jade *Huang* arc-shaped pendant, Jade *Chongya* and some jade fragments, was found on the waist of the owner of the tomb. These are typical representative burial objects of the Northern Dynasties (386–581 AD). The unearthed jade (Fig. 1a) has a three-layer or multi-layer structure, with a light green interior and a white spongy surface featuring various thicknesses. At the same time, there is a brown transition layer between the green inner layer and the white surface layer. Thus, optical microscopic analysis, X-ray diffraction analysis, scanning-energy spectrum analysis, microscopic three-dimensional imaging microscopic analysis, and organic matter analysis were carried out for the corrosion changes of the jade, so as to determine the cause of the corrosion, build a corresponding corrosion model, and provide new research ideas for the corrosion mechanism and protection of the unearthed jade.

Experiments

Sample

In order to systematically study the formation reason of the three-layer structure of the jade article, a jade fragment (Fig. 1b) was selected for experiment. The length, width and height of jade fragment was about 2 cm, 1.5 cm and 6 mm. The fragmentation of jade is formed by natural disintegration, and the excavated samples have not undergone all pretreatment including cutting. The PH of the soil around the sample burial is 8.3, the volume moisture content is 26.45%.

Methods

Optical microscopic analysis (OM)

The 4K digital microscope (Tianzhu Shanghai optical instrument factory XTZ-4KHD) was used to observe the microscopic morphology of the sample surface and cross-section formed by natural disintegration, and observations were made at 0.7 and 1.5 magnifications.

X-ray fluorescence spectroscopy analysis (XRF)

A German Bruker M4 Tornado plus microzone X-ray fluorescence imaging spectrometer was used to observe the corrosion layer on the sample surface and test its composition and distribution. XRF is a nondestructive test that only needs a plane without sample preparation and uses an X-ray tube; the target material is Rh, the FP method and type-calibration method are used, and a national standard ore sample is used to establish a quantitative

Fig. 1 **a** Unearthed jade; **b** OM images of the selected jade surface; **c** OM images of jade cross-section

method [24]. The accelerating voltage and beam currents were 50 kV and 600 μA, respectively.

Scanning electron microscopy equipped with energy-dispersive X-ray spectroscopy analysis (SEM-EDX)

The FEI Verios G4 field emission scanning electron microscope/energy spectrum was used to observe the microscopic morphologies of the corroded areas and cross sections of the sample fragments after platinum plating with ion sputtering and to perform compositional tests. Because the sample was fragile, the corrosion layer and cross-section of the sample surface was not polished. The voltage was set to 10 kV, and the working distance varied from 4.0 to 6.4 mm under vacuum conditions. The test results included secondary electron images and backscattered electron images.

X-ray diffraction analysis (XRD)

A Bruker D8 Advance X-ray diffractometer (Germany) was used to directly detect the three layers of the sample without preprocessing. The maximum voltage of the instrument was 60 kV, the maximum tube current was 80 mA, the optical tube power was 2.2 kW (Cu target), and the angle reproducibility was ± 0.0001°. A Vantec 500 two-dimensional surface detector with a test spot diameter of 0.5 mm and an integration time of 300 s was used.

Micron 3D stereo imaging microscope analysis (CT)

Zeiss MicroXCT-400 μm three-dimensional imaging microscope was used for three-dimensional non-destructive imaging of the sample and to study the microstructure and defects of the sample, including morphology, pores, cracks, and so on. The results are processed using Dragonfly Pro software. The maximum power of the light source is 10 W, and the maximum voltage is 140 kV. Additionally, the theoretical maximum resolution is 1 μm, and the maximum resolution of the CCD is 2048 * 2048.

Excitation-emission matrix spectroscopy analysis (EEMs)

HORIBA FluoroMax Plus steady state and lifetime benchtop spectrofluorometer was used to test the EEMs of the sample. The excitation wavelength range of 240–300 nm and the emission wavelength range of 330–700 nm were chosen to directly scan the luminous region of the sample without preprocessing. The scan sampling was set to 1 nm, and both excitation and emission slits were set to 5 nm. Subsequently, the raw measured spectral data were processed using FluorEssence software and result was drawn after deducting Rayleigh scattering.

Attenuated total reflectance-fourier transform infrared spectroscopy analysis (ATR-FTIR)

An American PerkinElmer Spotlight400 Fourier infrared spectrometer was used to test the corrosion layer of the sample, analyze the functional groups of the corrosion material, and determine the presence of organic matter in the sample. Infrared absorption spectroscopy was used to directly test the corrosion area on the surface of the sample without preprocessing. The test range was 500–4000 cm^{-1} with a spectral resolution better than 0.09 cm^{-1}, and the wavenumber accuracy was better than 0.01 cm^{-1}.

Results and discussion

Microscopic morphology and composition analysis

One of the jade fragments was taken for detailed analysis and it can be seen that there are three layers of distribution from OM at the cross-section of sample (Fig. 1c), including the surface white layer with thickness of about 1.5 mm, the brown intermediate layer with thickness of about 0.5 mm, and the inner matrix with thickness of about 3 mm. The elemental distribution on the cross-section of the sample was tested using the XRF surface scan mode, the test area was shown in Fig. 2a. It was observed, by comparing the distribution of elements in the sample, that the three layers all contain Ca, Mg and Si elements, and the enrichment of Mg, Si, Fe, and Ti elements was formed in the white layer on the surface of the sample, in which the Ca element was uniformly distributed in the inner matrix and surface white layer of the sample, while its content was relatively low in the brown intermediate layer. Furthermore, it could also be detected that obvious accumulation zones of S, P, and Al elements took shape in the brown intermediate layer region.

SEM-EDX and micro-area XRD were adopted to test and analyze the microscopic morphology of different regions, as well as the composition and structure of micro-area elements. Figure 3a–c indicate the microscopic morphology and distribution of constituent elements of the inner matrix, surface white layer, and the brown intermediate layer, respectively. Based on the element content and XRD spectrum, it was detectable that the jade matrix and the brown intermediate layer contained lizardite ($Mg_3Si_2(OH)_4O_5$) and calcite ($CaCO_3$) (Fig. 4a, c). Apart from that, the surface white layer was composed of not only calcite, but also antigorite ($Mg_6[Si_4O_{10}](OH)_8$) (Fig. 4b).

It is noticed, by comparing the microscopic morphology of different regions, that the lizardite and calcite inside the jade were lamellar with regular structure, while the structural composition of the brown intermediate layer and the surface white layer became scattered

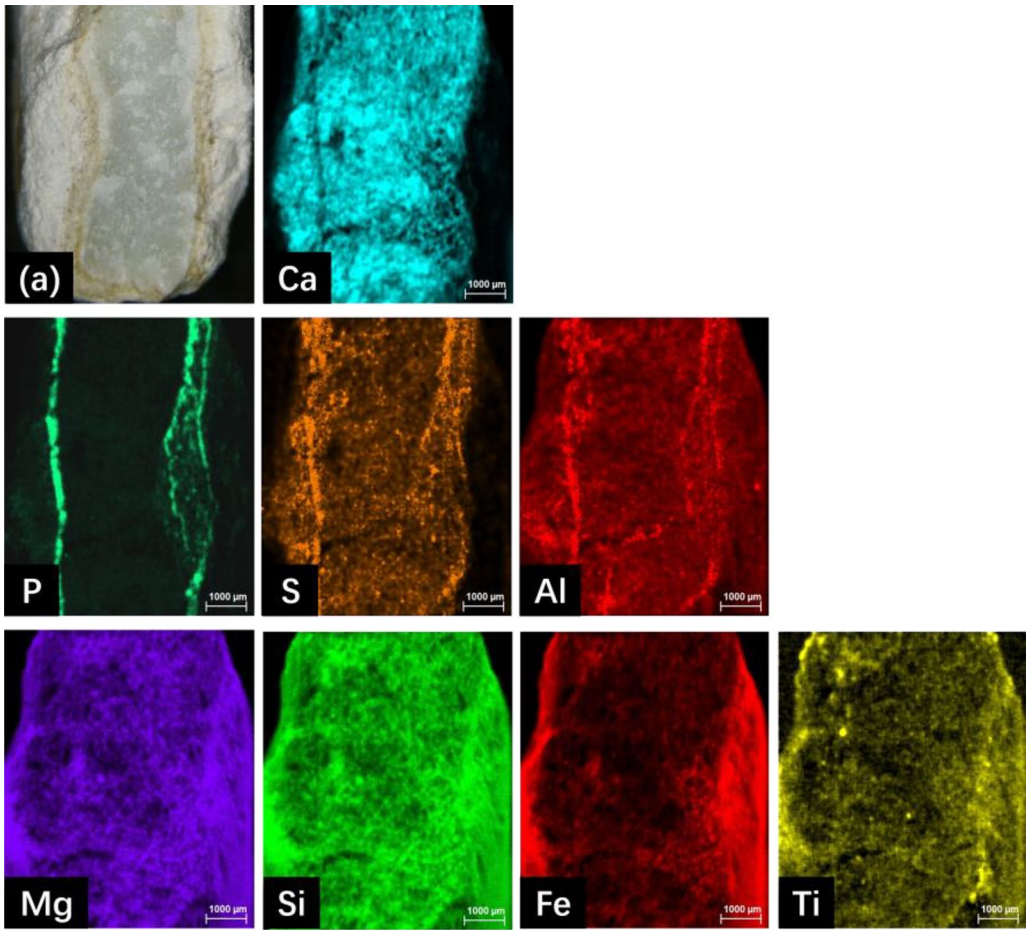

Fig. 2 XRF surface scan test results, **a** OM image of test area (the brighter the color is, the higher the element content, the same as below)

and irregular. Among them, the most obvious was that particles in the brown area were small and compact, and contained 1.74% of P element and 0.38% of S element, forming an obvious element aggregation zone. What is more, it was particularly evident from comparing the topographical regions of the inner and outer layers of the jade that the increase of Ca element mainly started from the junction area of the lamellar structure, with Mg and Si elements as the core, the surrounding elements gradually replaced by Ca elements, and the content of adsorbed C elements gradually increasing (Fig. 3a, b; Table 1).

Further, SEM-EDX was utilized to analyze the microscopic morphology and composition of different regions of the sample section. The results in Fig. 5; Table 2 manifested that the white layer on the surface of the jade included lamellar morphology structure, single-layer zigzag structure (Fig. 5a), and multi-layer zigzag structure (Fig. 5b). Among them, the single-layer (area P2 in Fig. 5a) and multi-layer (area P3 in Fig. 5b) serrated structures mainly composed of Ca and C were attached to the lamellar surface (P1) and contained a high content of C, i.e., 18.41% and 10.67%, respectively. From the comparison of the element content and the morphology in the figures, it could be deduced that calcium carbonate with a monolayer serrated structure was first formed on the lamellar layered surface; with the continuous increase of the content, the single-layer zigzag range gradually expanded and connected to each other, accumulating to form a multi-layer sawtooth structure such as that shown in Fig. 5b.

In the brown intermediate layer region (Fig. 5c), three different morphological structures appeared on the surface of the large plate-like matrix, including lamellar (area P4 in Fig. 5c), vermicular (area P5 in Fig. 5c), and reticular (area P6 in Fig. 5c) with high P element content. It was speculated, by comparing the change process and calculated the porosity by processing the images of different regions in Fig. 5 and estimating their scales, that the surface of the layered matrix of the large plate was firstly piled up with spherical nanoparticles of about 3 nm to form pores of 0.58%, and then the size of the spherical nanoparticles continued to increase, and the pores in the

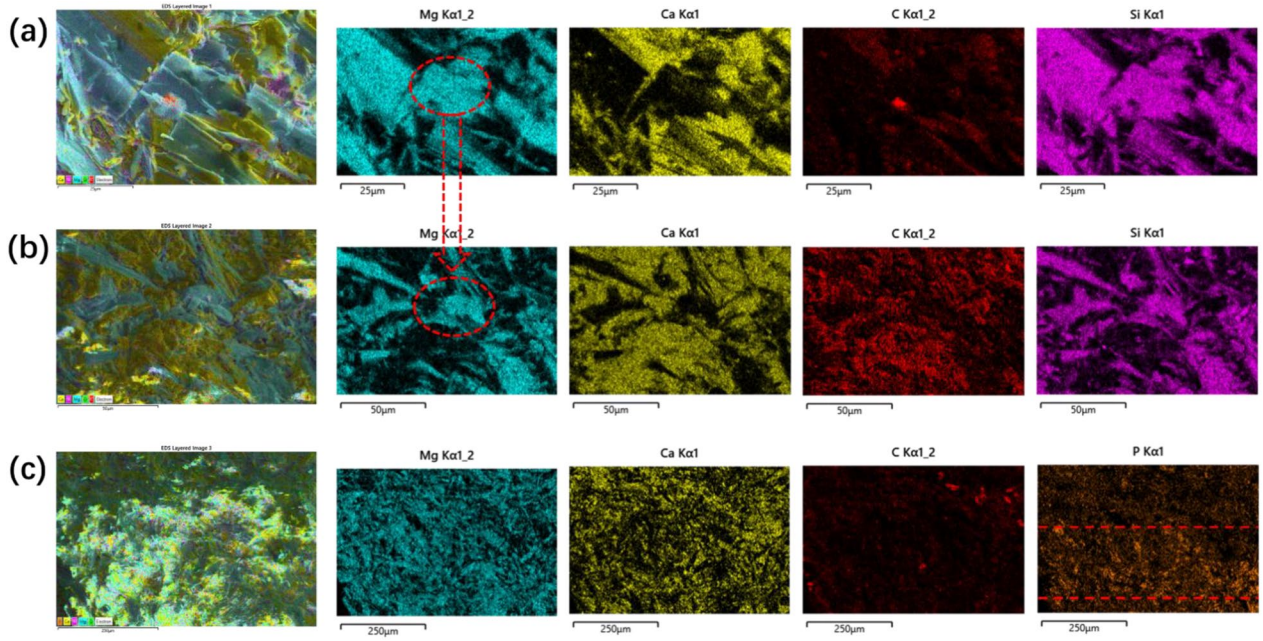

Fig. 3 SEM-EDX surface scanning test results of jade, **a** inner matrix; **b** surface white layer; **c** brown intermediate layer

same area increased to 4.47%, while the surface pores forming a reticular structure can be increased to 14.42%.

Following the above tests, it was found that the structure of each layer of the jade sample was quite different, and an obvious crack was formed between the brown intermediate layer and the inner matrix (Fig. 6). With the purpose of further determining the internal structure of the sample, CT was used to scan the sample internally, and the test results were shown in Fig. 7. In the white layer on the surface of the sample, there were many cracks that connected the brown intermediate layer with the outside and contained corrosion (shown by the arrow in Fig. 7). The 3D image information obtained from CT was imported into Dragonfly Pro software for image processing, it was calculated that the average porosity of the outermost white area was about 15.01%, and the distribution was uneven. The internal matrix was dense and uniformly distributed, but there were also cracks extending inward along the corrosion cracks.

Organic matter analysis

When comparing with the inner matrix of the uncorroded green jade, we noticed that the white layer on the surface and the brown intermediate layer contained elements such as C, S, and P. When the sample was irradiated with ultraviolet light, it was found that the brown intermediate layer showed an obvious fluorescence reaction at 365 nm purple light (shown by the arrow in Fig. 8). The experiment further used EEMs and ATR-FTIR to test the fluorescence effect and infrared spectrum curve of the surface.

Sample's EEMs was tested under the condition of excitation wavelength 240–300 nm and emission wavelength 340–700 nm, the experimental results is shown in Fig. 9, which demonstrated the intensity excitation of the fluorescence spectrum, the exact position of the emission wavelength, and the relative intensity. There are three strong spikes in the fluorescence spectra of the specific brown interlayer, and their excitation/emission bands were located at 240–245 nm/400–450 nm, 242–247 nm/510–570 nm, and 242–247 nm/670–700 nm respectively. Through the characterization of fluorescence spectra, it was determined that the broad and strong peak at 240–245 nm/400–450 nm was mainly produced by microorganisms, and UV humic acids with various fluorescent chromophores [25, 26]. The region of Em = 2 * Ex nm in the picture was a second-order Rayleigh signal (Em represents the emission spectrum and Ex represents excitation spectrum). The FluorEssence software was used to deduct Rayleigh scattering when drawing.

The soil where the cultural relics were buried contained organic matter that forms complex and stable macromolecular organic compounds under the action of microorganisms. Humus was the main component of soil organic matter, including carbon, hydrogen, oxygen, sulfur, phosphorus, and other elements. Humus serves as not a single organic compound, but a mixture of a series of organic

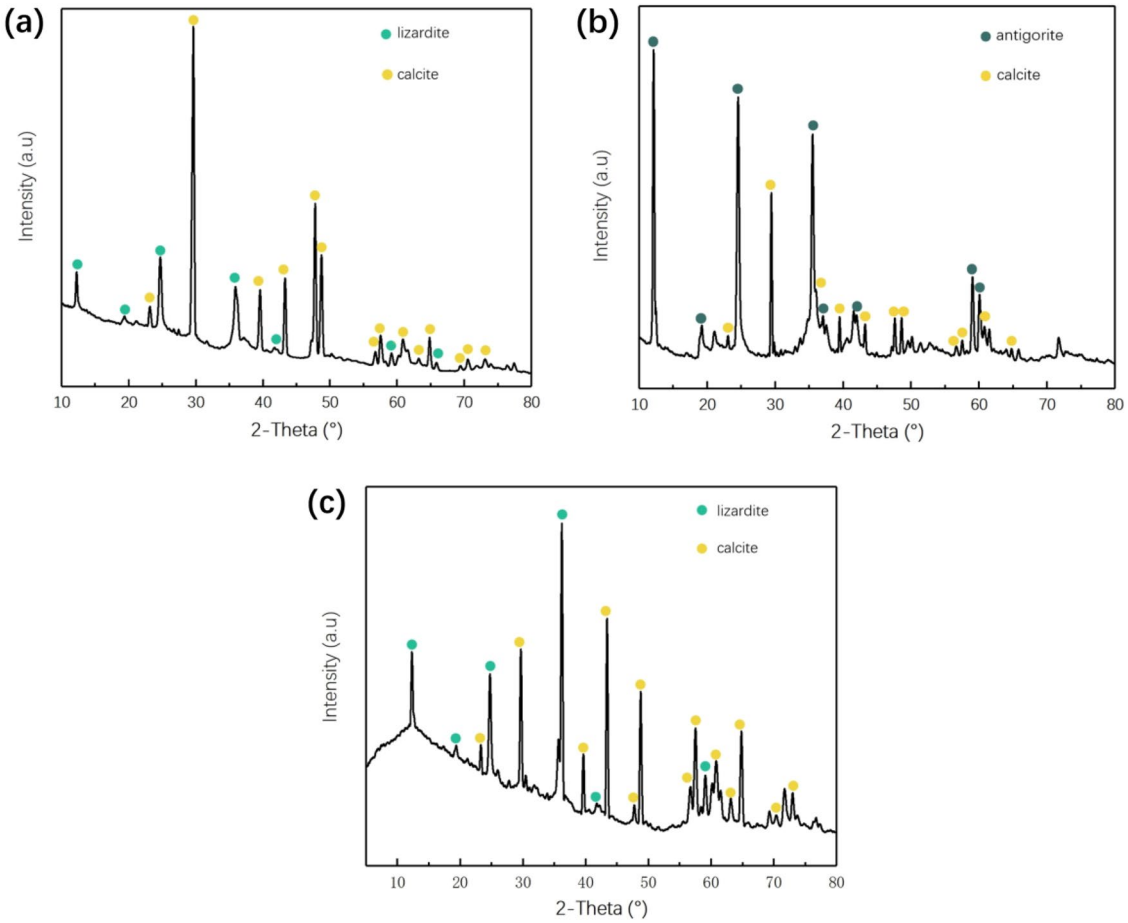

Fig. 4 XRD test results of different areas of jade, **a** inner matrix is lizardite and calcite; **b** surface white layer is antigorite and calcite; **c** brown middle layer is lizardite and calcite

Table 1 SEM-EDX test element composition of jade in different regions (wt%)

Element	C	O	Mg	Si	Ca	Fe	P	S
Inner matrix	9.32	52.29	14.73	11.32	11.88	0.46		
Surface white layer	11.38	52.97	10.42	7.80	17.10	0.33		
Brown intermediate layer	8.47	52.44	14.33	11.59	11.05		1.74	0.38

compounds with similarities and differences in composition, structure, and properties, which plays an essential role in promoting the decomposition of minerals and the release of compositions. Furthermore, it can exist in the state of free humic acid and humate in the soil, or it can combine closely with mineral clay in the form of gel to become an important colloid material [27–29].

In order to further determine the existence of organic matter in the humus, the infrared spectra of the brown intermediate layer and surface white layer of the sample were measured by ATR-FTIR, results are shown in Fig. 10. Among them, in the region of 400–1200 cm^{-1}, the infrared absorption bands were located at 1080 cm^{-1}, 995 cm^{-1}, 623 cm^{-1}, 565 cm^{-1} and 448 cm^{-1}. The 1080 cm^{-1} absorption band belongs to the SiO_4 tetrahedral Si–O_{nb} anti-symmetric stretching vibration, the 995 cm^{-1} strong absorption band belong to the symmetrical stretching vibration of the parallel structure layer of Si-O, the strong absorption band near 623 cm^{-1} and the absorption shoulder near 565 cm^{-1} belong to OH–Mg–OH translational motion, and the strong absorption band near 448 cm^{-1} belongs to Mg–OH translational motion.

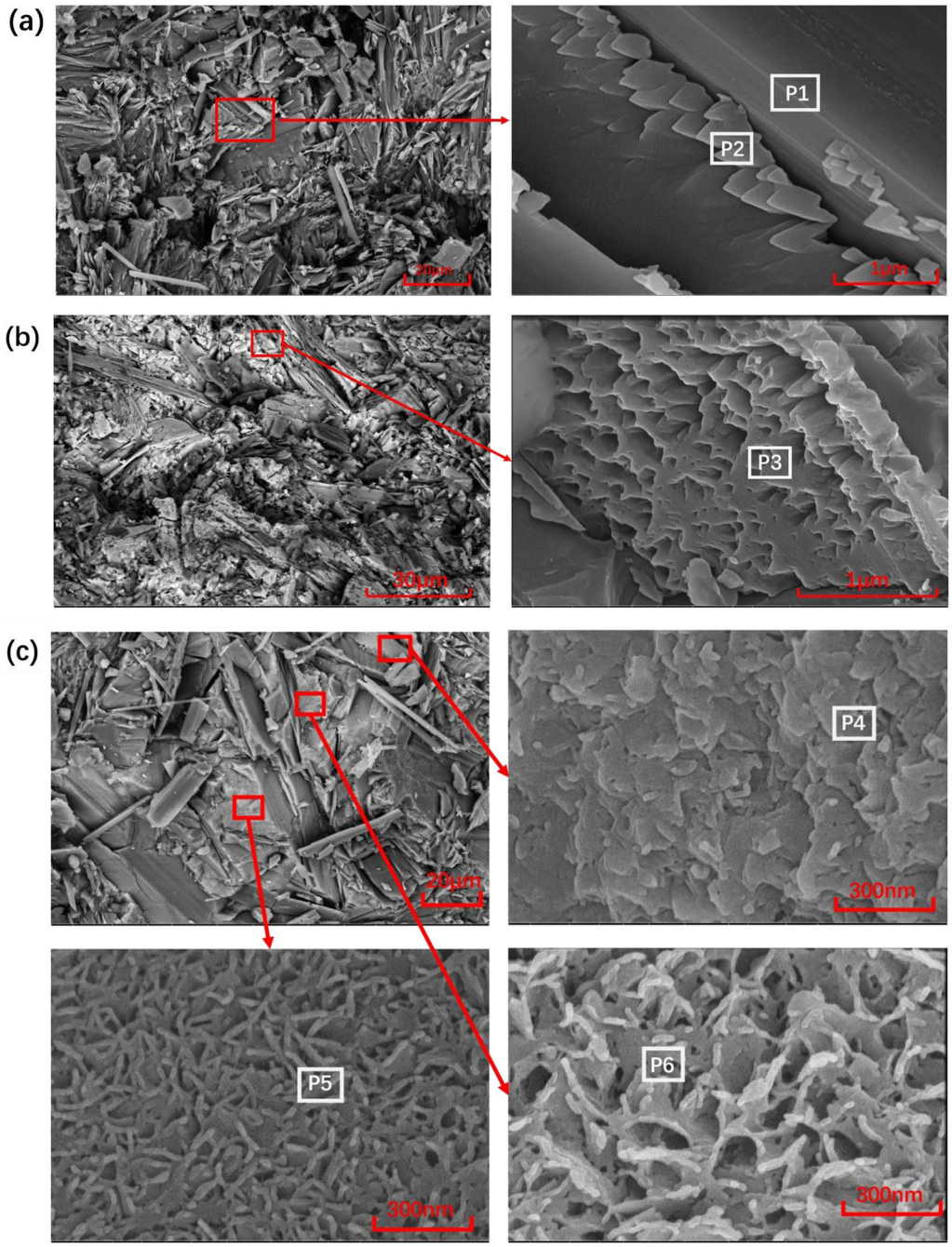

Fig. 5 SEM test images of jade, **a** sawtooth appearance of surface white layer; **b** multi-layer sawtooth appearance of surface white layer; **c** lamellar, vermicular and reticular appearances of brown intermediate layer

Meanwhile, in the region of 3620–3735 cm^{-1} in the spectral curve, 3715 cm^{-1} belong to the internal hydroxyl stretching vibration, and 3676 cm^{-1} belong to the external hydroxyl vertical stretching vibration, and 3655 cm^{-1} belong to the oblique stretching vibration of the outer hydroxyl [30, 31]. And three characteristic peaks at 1428 cm^{-1}, 876 cm^{-1} and 713 cm^{-1}, which are all related to CO_3^{2-} [32].

Different from the infrared spectrum curve of the white layer serpentine on the surface, the brown intermediate layer saw a wide –OH absorption peak at 3410 cm^{-1} [33], a characteristic symmetric and asymmetric stretching peaks of $–CH_2–$ and $–CH_3$ species at 2982 cm^{-1},

Table 2 SEM-EDX test element composition of jade in different regions (wt%)

Element	C	O	Mg	Si	P	Ca	Fe
P1	7.05	45.72	8.33	8.00		30.48	0.42
P2	18.41	60.65	4.51	2.81		13.62	
P3	10.67	48.85	5.43	3.87		31.18	
P4	5.44	46.84	2.34	1.05	13.35	30.72	0.26
P5	2.80	41.37	1.75	0.88	11.80	41.39	
P6	6.55	46.21	2.41	1.03	9.54	33.83	0.42

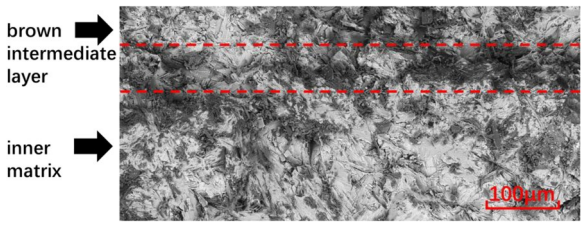

Fig. 6 SEM image of the transitional area between the inner matrix and the brown intermediate layer on the surface of jade

2921 cm^{-1}, and 2852 cm^{-1} [34], a ν(C=O) carboxylic acid or amide absorption peak at 1630 cm^{-1} [35], a stretching vibration of P–O and C–S or the stretching vibration of carboxyl C–O at 1228 cm^{-1} [36].

According to the distribution of elements on the surface of the sample, EEMs image, and infrared spectrum curve, it was determined that the brown intermediate layer of the sample had humic acid substances of microbial products, resulting in a strong fluorescence effect.

Corrosion mechanism

The lizardite that made up the jade contained OH magnesia layered silicate, with the structural unit layer composed of the silicon-oxygen tetrahedron and magnesia octahedron at 1:1. The internal connection of silicon-oxygen tetrahedron was a covalent bond, and that of magnesia octahedron was a weak ionic bond, in which Mg was connected with a hydroxyl group and reactive oxygen species in a silicon-oxygen tetrahedron, and the unit layers were connected by weak hydrogen bond or Van der Waals' force [37, 38].

Humus was randomly produced from plant tissue decay or microbial metabolism-catabolism or a mixture of both [39]. Microorganisms played a vital role in the formation of humic acid, as soil-humic acid-microorganisms were inseparable, and most of the biologically essential elements required to maintain microbial growth and metabolism are originally derived from minerals [40].

The corrosion process of jade was presented in Fig. 11. When serpentine jade was buried in the soil and closely integrated with the gel-like humic acid produced by soil microorganisms, humic acid promoted the decomposition of minerals, the release of components, and had strong permeability. The OH-containing magnesium

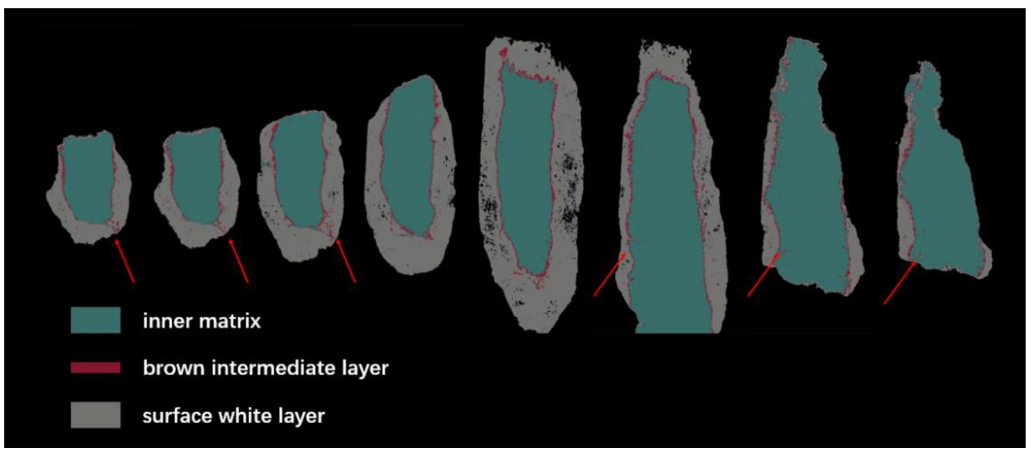

Fig. 7 2D images of the cross-section of the jade CT test

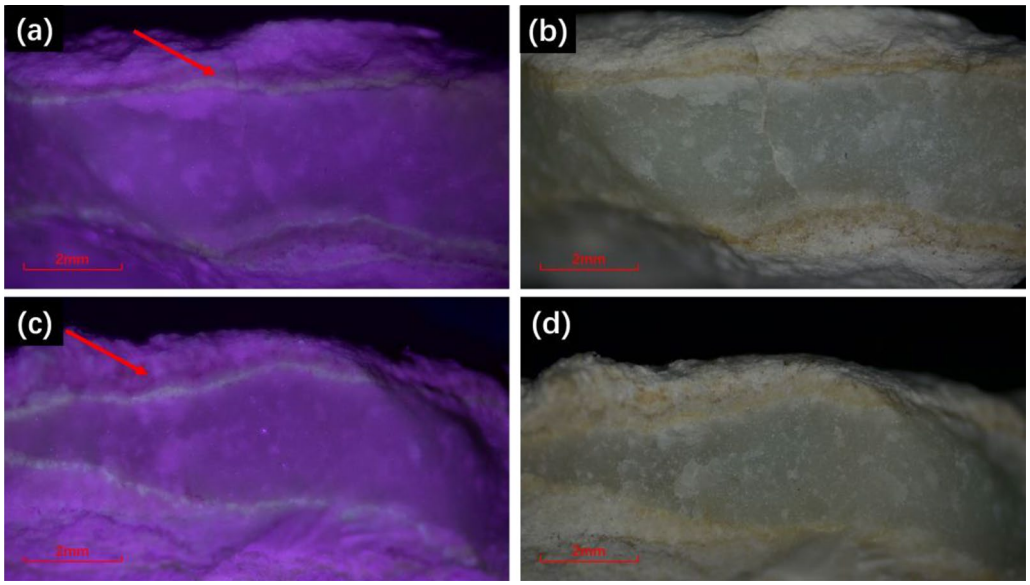

Fig. 8 Fluorescence reaction of the brown intermediate layer of jade under the irradiation of 365 nm purple light, **a**, **c** 365 nm purple light; **b**, **d** natural light (the white layer in **a** and **c** are fluorescent areas)

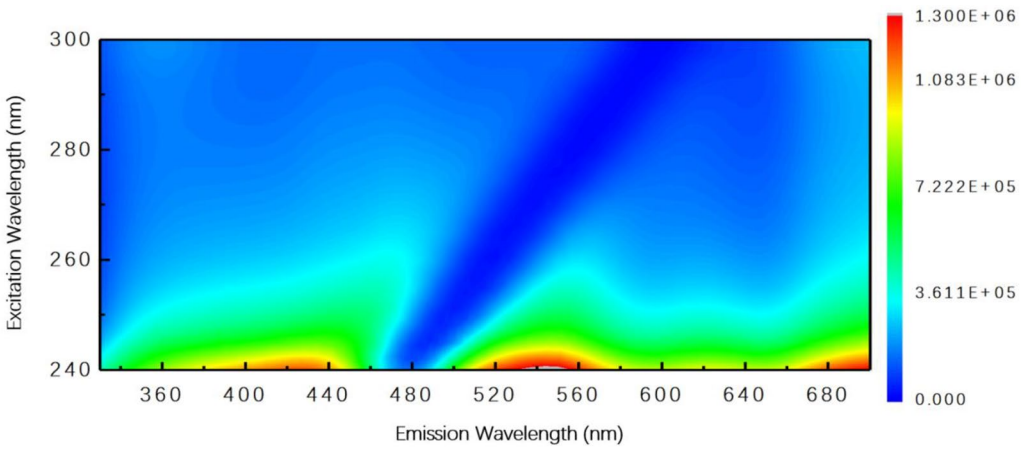

Fig. 9 EEMs of jade at an excitation wavelength of 240–300 nm, and emission wavelength of 340–700 nm

silicate crystal structure that was made up of jade was decomposed and destroyed layer by layer from the surface to the inside. First of all, after the magnesium hydroxide layer of serpentine became in contact with humic acid, the local microenvironment was formed leading to the rapid dissolution and release of Si, Mg and Fe ions of the network skeleton, especially the Mg ion groups, and the dissolution of soluble magnesium. Afterward, the [SiO_4] layer that is difficult to decompose would also produce soluble silicon to dissolve and exchange with H^+ in the solution, resulting in the Si–O–Si bond fracture of the network structure [41]. Iron oxide would also dissolve and precipitate slowly under local acidic conditions, and Si, Mg, Fe, and other elements that are easy to dissolve under acidic conditions penetrate upward to the dissolved part of the jade and accumulate on the corroded surface (Fig. 11b).

The vacancy region produced by the dissolution of Si and Mg ions was replaced by Ca ions, with Mg and Si elements as the core, the surrounding elements gradually replaced by Ca elements, and the content of adsorbed C element increased gradually (Fig. 11c). This part of the change was presumed to be due to the adsorption of humic acid on the surface of jade, constructing

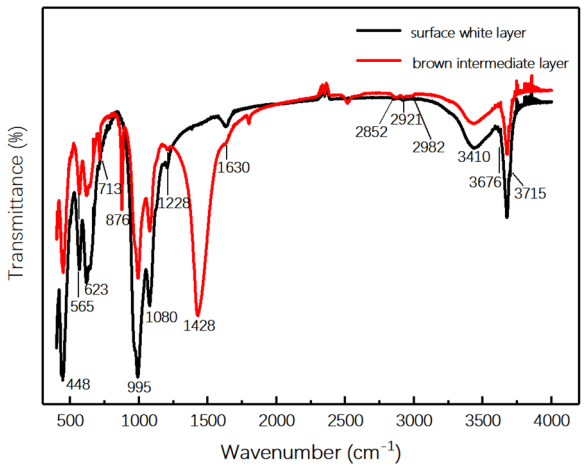

Fig. 10 ATR-FTIR test results of brown intermediate layer of jade

a micro-reaction environment, which determined the nucleation site of mineralized inorganic substances and the function of mineral formation. Subsequently, the inorganic ions nucleated, grew, and aggregated at the inorganic–organic interface through electrostatic force, chelation, hydrogen bond, VDW, etc. in the generated acidic solution, forming unevenly distributed calcified products [18–20]. Humic acid would continuously infiltrate into the jade along the cracks of the loose outer layer, dissociate and enrich at the corrosion interface to form brown bands (Fig. 11d). Meanwhile, there were certain P and S elements in microorganisms and extracellular polymers (EPS) or organic components of the medium in humic acid [42–45], and amphoteric oxides containing Al were also affected and enriched in the corrosion zone [46]. Obvious aggregation bands of P, S, and Al elements were formed at the brown corrosion interface (Fig. 11e). As a matter of fact, there were a large number of micro- and nano-pores in this area, and the corrosion interface had a more ordered mesoporous structure, and the larger specific surface area also showed faster reaction activity, which promoted the continuous occurrence of corrosion.

Since the structure of the corrosion area was disorderly and non-directional, the bonding between different phases deteriorated and the distribution became scattered; the interface with the original jade matrix was apparent, and this part was more susceptible to corrosion by external corrosive solutions such as humic acid, which further resulted in corrosion and biomineralization. In a word, the corrosion of magnesium-silicon serpentine with a lamellar structure was closely related to the fluorescent humic acid contained in the buried microenvironment.

Conclusion

In this paper, analyses regarding the microscopic morphology, composition and structure of the jade fragment of unearthed aristocratic Daye Zhen Tomb of the

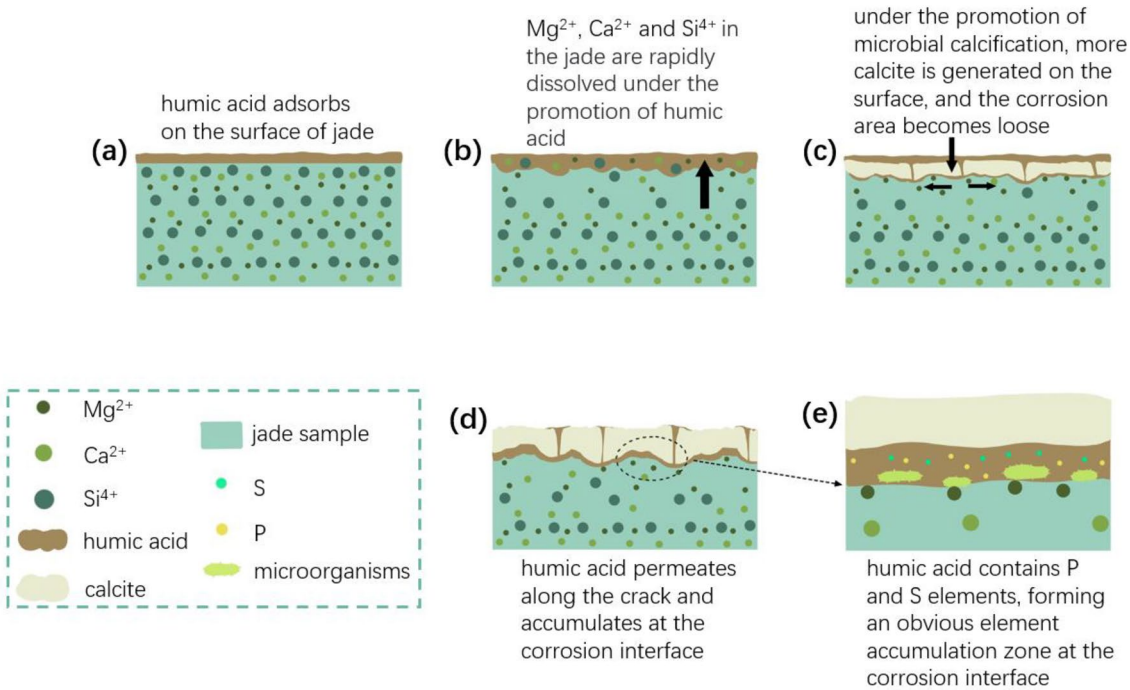

Fig. 11 Schematic diagram of jade corrosion

Northern Zhou Dynasty were conducted, in which the structure of the surface white layer was more scattered and irregular than that of the inner matrix, and the content of calcite increased significantly. Meanwhile, there was an obvious gap between the corroded area and the uncorroded area. Furthermore, there was an accumulation zone of P, S, and Al elements with a significant fluorescence effect between the inner matrix and the surface white layer. After testing, it was determined that the accumulation zone was humus, and the humus continuously infiltrated into the jade along the cracks of the loose outer layer, dissociated and enriched at the corrosion interface, forming a macroscopically visible brown intermediate layer band.

The main cause of the formation of a white corrosion layer on the surface of the jade could be attributed to the change of structure and the increase of calcite content, which was speculated to be formed by ion exchange and biomineralization of microorganisms in humus, as humic acid infiltrated into the internal corrosion interface of jade and accelerated the corrosion of magnesite-silicon serpentine with lamellar structure. In this paper, the humic acid zone with corrosion and fluorescence effect in serpentine was identified for the first time, which plays a rather crucial role in jade corrosion. This study also prompts to the attention on the microbial corrosion in jade, which needs further investigation in the future.

Acknowledgements
Not applicable.

Author contributions
KZ: conceptualization, data collection, writing—original draft preparation. YZ: methodology, resources. JZ: supervision, writing—review and editing, funding acquisition. ZZ and MZ: investigation, data curation. XZ and HL: conceptualization, supervision. All authors read and approved the final manuscript.

Funding
This research was financially supported by the National Natural Science Foundation of Shanghai in China (No. 20ZR1422800, No. 23ZR1421000).

Availability of data and materials
All data generated or analysed during this study are included in this published article and its Additional files.

Declarations

Competing interests
The authors declare no competing interests.

Received: 25 June 2023 Accepted: 13 October 2023
Published online: 23 October 2023

References

1. Wang R. Progress review of the scientific study of Chinese ancient jade. Archaeometry. 2011;53:674–92. https://doi.org/10.1111/j.1475-4754.2010.00564.x.
2. Wang R, Li YF. Jade and precious stones. Ref Mod Soc Sci. 2023. https://doi.org/10.1016/B978-0-323-90799-6.00110-5.
3. Harlow GE, Sorensen SS. Jade (nephrite and jadeitite) and serpentinite: metasomatic connections. Int Geol Rev. 2005;47:113–46. https://doi.org/10.2747/0020-6814.47.2.113.
4. Harlow GE, Tsujimori T, Sorensen SS. Jadeitites and plate tectonics. Annu Rev Earth Planet Sci. 2015;43:105–38. https://doi.org/10.1146/annurev-earth-060614-105215.
5. Wang R, Wang CS, Tang JG. A jade parrot from the tomb of Fu Hao at Yinxu and Liao sacrifices of the Shang Dynasty. Antiquity. 2018;92:368–82. https://doi.org/10.15184/aqy.2017.220.
6. Wang R, Mai YY, Lin LG. Burnt jade sacrifices in the Chinese neolithic: the Liangzhu cemetery at Sidun. Antiquity. 2023;96:1495–514. https://doi.org/10.15184/aqy.2022.101.
7. Kundu TK, Rao KH, Parker SC. Atomistic simulation of the surface structure of wollastonite. Chem Phys Lett. 2003;377:81–92. https://doi.org/10.1016/S0009-2614(03)01097-2.
8. Yu CJ, Kundin J, Cottenier S, Emmerich H. Ab initio modeling of glass corrosion: hydroxylation and chemisorption of oxalic acid at diopside and akermanite surfaces. Acta Mater. 2009;57:5303–13. https://doi.org/10.1016/j.actamat.2009.07.023.
9. Du JC, Cormack AN. Molecular dynamics simulation of the structure and hydroxylation of silica glass surfaces. J Am Ceram Soc. 2015;88:2532–9. https://doi.org/10.1111/j.1551-2916.2005.00352.x.
10. Snellings R. Surface chemistry of calcium aluminosilicate glasses. J Am Ceram Soc. 2015;98:303–14. https://doi.org/10.1111/jace.13263.
11. Hellmann R, Dran JC, DellaMea G. The albite–water system: part III. Characterization of leached and hydrogen-enriched layers formed at 300°C using MeV ion beam techniques. Geochim Cosmochim Acta. 1997;61:1575–94. https://doi.org/10.1016/S0016-7037(97)00022-7.
12. Li Z, Xiao TL, Pan QY, Cheng JM, Zhao SG. Corrosion behaviour and mechanism of basalt fibres in acidic and alkaline environments. Corros Sci. 2016;110:15–22. https://doi.org/10.1016/j.corsci.2016.04.019.
13. Kamennaya NA, Ajo-Franklin CM, Northen T, Jansson C. Cyanobacteria as biocatalysts for carbonate mineralization. Minerals. 2012;2:338–64. https://doi.org/10.3390/min2040338.
14. Singh MR, Ganaraj K, Sable PD. Surface mediated Ca-phosphate biomineralization and characterization of the historic lime mortar, Janjira Sea Fort, India. J Cult Herit. 2020;44:110–9. https://doi.org/10.1016/j.culher.2020.02.004.
15. Sun B, Zhao H, Zhao YH, Tucker ME, Han ZZ, Yan HX. Bio-precipitation of carbonate and phosphate minerals induced by the bacterium citrobacter freundii ZW123 in an anaerobic environment. Minerals. 2020. https://doi.org/10.3390/min10010065.
16. Xiao LL, Lian B, Hao JC, Liu CQ, Wang SJ. Effect of carbonic anhydrase on silicate weathering and carbonate formation at present day CO_2 concentrations compared to primordial values. Sci Rep. 2015. https://doi.org/10.1038/srep07733.
17. Wang YA, Zhang RY, Duan JZ, Shi X, Zhang YM, Guan F, Sand W, Hou BR. Extracellular polymeric substances and biocorrosion/biofouling: recent advances and future perspectives. Int J Mol Sci. 2022. https://doi.org/10.3390/ijms23105566.
18. Spadafora A, Perri E, McKenzie JA, Vasconcelos C. Microbial biomineralization processes forming modern Ca: Mg carbonate stromatolites. Sedimentology. 2010;57:27–40. https://doi.org/10.1111/j.1365-3091.2009.01083.x.
19. Pace A, Bourillot R, Bouton A, Vennin E, Galaup S, Bundeleva I, Patrier P, Dupraz C, Thomazo C, Sansjofre P. Microbial and diagenetic steps leading to the mineralisation of Great Salt Lake microbialites. Sci Rep. 2016;6:6. https://doi.org/10.1038/srep31495.
20. Liu HW, Gu TY, Asif M, Zhang GA, Liu HF. The corrosion behavior and mechanism of carbon steel induced by extracellular polymeric substances of iron-oxidizing bacteria. Corros Sci. 2018;114:102–11. https://doi.org/10.1016/j.corsci.2016.10.025.
21. Perri E, Tucker ME, Slowakiewicz M, Whitaker F, Bowen L, Perrotta ID. Carbonate and silicate biomineralization in a hypersaline microbial mat (Mesaieed Sabkha, Qatar): roles of bacteria, extracellular polymeric substances and viruses. Sedimentology. 2018;65:1213–45. https://doi.org/10.1111/sed.12419.
22. He JQ, Tan Y, Liu HX, Jin ZY, Zang YX, He FX, Yan ZX, Liu HF, Meng GZ, Liu HW. Extracellular polymeric substances secreted by marine fungus

Aspergillus terreus: full characterization and detailed effects on aluminum alloy corrosion. Corros Sci. 2022. https://doi.org/10.1016/j.corsci.2022.110703.
23. De Wit Z, Gautret P, Bettarel Y, Roques C, Marliere C, Ramonda M, Thanh TN, Quang HT, Bouvier T. Viruses occur incorporated in biogenic high-Mg calcite from hypersaline microbial mats. PLoS ONE. 2015. https://doi.org/10.1371/journal.pone.0130552.
24. Yuryeva TV, Malykhin SA, Kudryavtsev AA, Afanasyev IB, Kadikova IF, Yuryev VA. CdZnSSe crystals synthesized in silicate glass: structure, cathodoluminescence, band gap, discovery in historical glass, and possible applications in contemporary technology. Mater Res Bull. 2022. https://doi.org/10.1016/j.materresbull.2019.110704.
25. Chen W, Westerhoff P, Leenheer JA, Booksg K. Fluorescence excitation-emission matrix regional integration to quantify spectra for dissolved organic matter. Environ Sci Technol. 2003;37:5701–10. https://doi.org/10.1021/es034354c.
26. Zhou J, Wang JJ, Baudon A, Chow AT. Improved fluorescence excitation-emission matrix regional integration to quantify spectra for fluorescent dissolved organic matter. J Environ Qual. 2013;42:925–30. https://doi.org/10.2134/jeq2012.0460.
27. Li H, Li Y, Li C. Characterization of humic acids and fulvic acids derived from sewage sludge. Asian J Chem. 2013;25:10087–91. https://doi.org/10.14233/ajchem.2013.15162.
28. Wang YK, Hao XZ, Wang YJ, Zhou DM, Zhang HC. Characteristics and mechanisms of Pb(II)adsorption on palygorskite-humic acid complex. J Agro-Environ Sci. 2009;28:2324–7. https://doi.org/10.3321/j.issn:1672-2043.2009.11.020.
29. Sutton R, Sposito G. Molecular structure in soil humic substances: the new view. Environ Sci Technol. 2005;39:9009–16. https://doi.org/10.1021/es050778q.
30. Trittschack R, Grobety B, Koch-Muller M. In situ high-temperature Raman and FTIR spectroscopy of the phase transformation of lizardite. Am Min. 2012;97:1965–76. https://doi.org/10.2138/am.2012.4162.
31. Balan E, Saitta AM, Mauri, Lemaire C, Guyot F. First-principles calculation of the infrared spectrum of lizardite. Am Min. 2002;87:1286–90. https://doi.org/10.2138/am-2002-1003.
32. Zhu Y, Li YZ, Lu AH, Ding HR, Li Y, Wang CQ. Middle and far infrared spectroscopic analysis of calcite, dolomite and magnesite. Earth Sci Front. 2022;29:459–69. https://doi.org/10.13745/j.esf.sf.2021.1.58.
33. Doroshenko I, Pogorelov V, Sablinskas V, Balevicius V. Matrix-isolation study of cluster formation in methanol O–H stretching region. J Mol Liq. 2010;157:142–5. https://doi.org/10.1016/j.molliq.2010.09.003.
34. Brownson JRS, Tejedor-Tejedor MI, Anderson MA. FTIR spectroscopy of alcohol and formate interactions with mesoporous TiO_2 surfaces. J Phys Chem B. 2006;110:12494–9. https://doi.org/10.1021/jp0614547.
35. Wu WH, Liu ZP, Fang F, Shi P, Cheng J. Characteristic of dissolved organic matter in leachate during SBR-coagulation treatment process. Chin J Environ. 2015;9:1124–30. https://doi.org/10.12030/j.cjee.20150322.
36. Han RP, Bao GL, Zhu L. Comparison of infrared spectra of native and esterified beer yeast. Spectrosc Spectr Anal. 2004;24:820–2. https://doi.org/10.3321/j.issn:1000-0593.2004.07.014.
37. Hilairet N, Daniel I, Reynard B. P–V equations of state and the relative stabilities of serpentine varieties. Phys Chem Miner. 2006;33:629–37. https://doi.org/10.1007/s00269-006-0111-0.
38. Bleam WF. Atomic theories of phyllosilicates: quantum chemistry, statistical mechanics, electrostatic theory, and crystal chemistry. Rev Geophys. 1993;31:51–73. https://doi.org/10.1029/92RG01823.
39. Piccolo A. The supramolecular structure of humic substances: a novel understanding of humus chemistry and implications in soil science. Adv Agron. 2002;75:57–134. https://doi.org/10.1016/S0065-2113(02)75003-7.
40. Moore EK, Jelen BI, Giovannelli D, Raanan H, Falkowski PG. Metal availability and the expanding network of microbial metabolisms in the Archaean eon. Nat Geosci. 2017;10:629–36. https://doi.org/10.1038/NGEO3006.
41. Bunker BZ. Molecular mechanisms for corrosion of silica and silicate glasses. J Non-Cryst Solids. 1994;179:300–8. https://doi.org/10.1016/0022-3093(94)90708-0.
42. Zelles L. Fatty acid patterns of phospholipids and lipopolysaccharides in the characterisation of microbial communities in soil: a review. Biol Fertil Soils. 1999;29:111–29. https://doi.org/10.1007/s003740050533.
43. Turner BL, Condron LM, Richardson SJ, Peltzer DA, Allison VJ. Soil organic phosphorus transformations during pedogenesis. Ecosystems. 2007;10:1166–81. https://doi.org/10.1007/s10021-007-9086-z.
44. Zhong YJ, Wen HG, Chen HD, Liu L, Chen AQ, Wang XL, Wang ZW, Bai X. The role of extracellular polymeric substances in cyanobacterial calcification and its geological significance. Acta Seismol Sin. 2022;40:88–105. https://doi.org/10.14027/j.issn.1000-0550.2020.102.
45. Vu B, Chen M, Crawford RJ, Ivanova EP. Bacterial extracellular polysaccharides involved in biofilm formation. Molecules. 2009;14:2535–54. https://doi.org/10.3390/molecules14072535.
46. Puttamraju P, SenGupta AK. Evidence of tunable on–off sorption behaviors of metal oxide nanoparticles: role of ion exchanger support. Ind Eng Chem Res. 2006;45:7737–42. https://doi.org/10.1021/ie060803g.

Publisher's Note